Available online at www.sciencedirect.com
ScienceDirect
Journal of Computational Physics 223 (2007) 690–710
JOURNAL OF COMPUTATIONAL PHYSICS
www.elsevier.com/locate/jcp

Perfectly matched layers in photonics computations: 1D and 2D nonlinear coupled mode equations

Tomáš Dohnal [a,*], Thomas Hagstrom [b]

[a] *Seminar for Applied Mathematics, ETH-Zentrum, CH-8092, Zürich, Switzerland*
[b] *Department of Mathematics and Statistics, University of New Mexico, Albuquerque, NM 87131, USA*

Received 13 July 2006; received in revised form 29 September 2006; accepted 2 October 2006
Available online 14 November 2006

Abstract

Extending the general approach for first-order hyperbolic systems developed in [D. Appelö, T. Hagstrom, G. Kreiss, Perfectly matched layers for hyperbolic systems: general formulation, well-posedness and stability, SIAM J. Appl. Math., 2006, to appear], we construct PML equations for the mixed-type system governing propagation of optical wave packets in both 1D and 2D Bragg resonant photonic waveguides with a cubic nonlinearity, i.e. the coupled mode equations. We prove that in the linear case the layer equations are absorbing and perfectly matched. We also prove they are stable for constant parameters. A number of numerical experiments are performed to assess the layer's performance in both the linear and nonlinear regimes.

1. Introduction

Realistic wave propagation problems are ubiquitously dispersive and their numerical simulations have to, therefore, typically treat modes (waves) that, within the integration time, travel out of the spatial domain of interest. This treatment needs to be efficient, to automatically and accurately treat all such modes, that is it should only introduce minimal artificial reflections. Two basic approaches have been developed for such problems, the perfectly matched layers (PML) and radiation boundary conditions, of which we use the former one in our model.

In nonlinear optics problems, when modeling the evolution of solitary waves (or solitons) in the presence of radiation due to, for instance, perturbations or solitary wave interactions, the radiation propagates at a larger group velocity than the solitary wave. Treatment of radiation leaving the domain is then essential [27,28]. In such cases the main part of the solution, i.e. the solitary wave, remains in the physical domain and only the typically small radiation enters the layers. Despite the nonlinearity of the system the dynamics in the layers are, therefore, linear and a linear PML may be used. In the presence of solitons propagating at different

* Corresponding author.
E-mail addresses: dohnal@math.ethz.ch (T. Dohnal), hagstrom@math.unm.edu (T. Hagstrom).

0021-9991/$ - see front matter
doi:10.1016/j.jcp.2006.10.002

velocities one of the solitons itself may leave the domain within the time of interest and PML has been used in order to minimize its unphysical reflection from the boundary [12,14,27]. (For information on radiation boundary conditions for the Schrödinger equation see e.g. [13,20,22].)

This paper derives and tests PML for a wave propagation problem in both 1D and 2D optical nonlinear Bragg resonant grating waveguides. The Bragg grating [25] is a special periodic structure leading to coupling between forward and backward (along the periodicity direction) propagating waves, and in combination with the (cubic) nonlinearity leads to the existence of localized solitary waves with a large range of velocities [2,4,10,11]. Simulations of slow solitary waves may result in the need for very large evolution times and thus for good long time behavior of the PML. See, for example [10,11], where interactions of 2D solitary waves with spatially localized defects are simulated (with the help of PML) up to $t \approx 1000$ for solitary waves travelling at speeds around 0.2 and the radiation at velocities in $(-1, 1)$ depending on the wavenumber.

The PML formulation is typically, and also here, derived for linear equations with the expectation of satisfactory performance even in presence of (e.g. polynomial) nonlinear terms under the condition that the solution remains small inside the absorbing layers. Although the split-field PML approach for the Maxwell's equation has been adapted for the presence of nonlinear terms via an iterative scheme [26], we use the (unsplit and more rigorous) linear approach for general first order hyperbolic systems [5,17,18], which we extend for the governing coupled mode equations (CME). This system is hyperbolic in the 1D case and of degenerate Schrödinger type in the 2D case, taking the form of a first-order hyperbolic equation in one of the two spatial dimensions.

The rest of the paper is organized as follows. In Section 2, we present the partial differential equations governing the physical model at hand and introduce some necessary notation. In Sections 3–5, we present a detailed derivation of the PML equations (for both 1D and 2D linear CME) using elementary intuitive arguments to prove their absorption and perfect matching. Section 6 contains a proof of stability of the PML equations. Finally, in Section 7 we present a number of numerical tests in both one and two dimensions showing exponential error convergence with respect to the width of the absorbing layers.

2. The main equations and notation

We address the propagation of quasi-monochromatic wavepackets of light in two-dimensional optical dielectric waveguides with a Bragg resonant spatially periodic structure (so-called Bragg grating [25]) in the propagation direction and a homogeneous structure in the transverse direction. If the underlying medium possesses the cubic focusing nonlinearity, then the wave propagation is modeled by the 2D coupled mode equations [1,4,10,11], which in their nondimensional form read

$$\begin{aligned} &\mathrm{i}(\partial_t + c_g\partial_z)E_+ + \kappa E_- + \partial_x^2 E_+ + \Gamma(|E_+|^2 + 2|E_-|^2)E_+ = 0,\\ &\mathrm{i}(\partial_t - c_g\partial_z)E_- + \kappa E_+ + \partial_x^2 E_- + \Gamma(|E_-|^2 + 2|E_+|^2)E_- = 0, \end{aligned} \tag{1}$$

where E_+ and E_- denote the forward and backward (in z) propagating wavepackets, respectively, c_g, κ, $\Gamma > 0$ are proportional to the group velocity, grating depth and the cubic susceptibility of the medium, respectively, and x, z and t correspond to the coordinate along the transverse direction, the propagation direction and time, respectively. The dynamics in the third spatial direction y are assumed stationary due to total internal reflection. The coexistence and coupling of forward and backward propagating wavepackets is caused by the Bragg resonant structure.

The corresponding one-dimensional model is the system of 1D coupled mode equations (Eqs. (1) without the ∂_x^2 terms). It describes the same situation in the fiber grating, where total internal reflection confines the dynamics in all transverse directions. Much more research has been historically devoted to this 1D model [2,6,7,15,23,25] but to our knowledge systematic treatment of radiation in numerical simulations appears in the literature neither for 1D nor for 2D.

As they stand, Eqs. (1) are defined on the whole plane $(x, z) \in \mathbb{R}^2$. For computational purposes we consider a finite domain $(x, z) \in [0, L_x] \times [0, L_z]$ appended with absorbing layers in the x-direction $[-\delta_x, 0] \times [0, L_z]$ and $[L_x, L_x + \delta_x] \times [0, L_z]$, in the z-direction $[0, L_x] \times [-\delta_z, 0]$ and $[0, L_x] \times [L_z, L_z + \delta_z]$ and in the corners $[-\delta_x, 0] \times [-\delta_z, 0]$, $[-\delta_x, 0] \times [L_z, L_z + \delta_z]$, $[L_x, L_x + \delta_x] \times [-\delta_z, 0]$ and $[L_x, L_x + \delta_x] \times [L_z, L_z + \delta_z]$, see Fig. 1. Note that the initial data are assumed to be supported only on the physical domain $[0, L_x] \times [0, L_z]$.

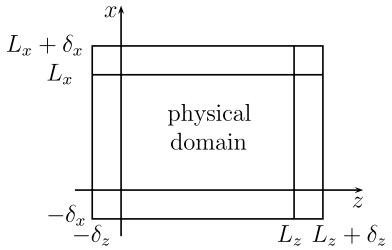

Fig. 1. The physical domain and the absorbing layers.

We use the linear case of Eqs. (1), i.e. $\Gamma = 0$, to derive the layer equations. The resulting system is then used even in the nonlinear case $\Gamma > 0$ under the condition that inside the layers the solution remains small in magnitude so that the dynamics are essentially linear. We also show one example when an $\mathcal{O}(1)$ disturbance propagates into the layer in the nonlinear case; this results in a largely increased error and decreased convergence rate.

In the following calculations the negative real semiaxis is chosen as the branch cut of the square root function and for $\xi = re^{i\theta}$, $\theta \in [-\pi, \pi)$, $r > 0$ we use $\xi^{1/2}$ or $\sqrt{\xi}$ to denote $\sqrt{r}e^{\theta/2}$ and $-\xi^{1/2}$ or $-\sqrt{\xi}$ to denote $\sqrt{r}e^{\theta/2+\pi}$.

3. z-Layer equations

To derive equations in the z-layers $[0, L_x] \times [-\delta_z, 0]$ and $[0, L_x] \times [L_z, L_z + \delta_z]$, see Fig. 2, we first perform the Laplace transform in t over $[0, \infty)$ and Fourier transform in x over $(-\infty, \infty)$ on the linear case of (1). For z outside the physical domain $[0, L_z]$ we obtain

$$\begin{aligned} &ic_g \partial_z \hat{E}_+ + (is - k_x^2)\hat{E}_+ + \kappa \hat{E}_- = 0, \\ &-ic_g \partial_z \hat{E}_- + (is - k_x^2)\hat{E}_- + \kappa \hat{E}_+ = 0, \end{aligned} \tag{2}$$

where we have used the fact that $E_\pm(t = 0) \equiv 0$ in the layers $z < 0$ and $z > L_z$. (2) has solution modes $(\hat{E}_+, \hat{E}_-) = (c_1, c_2)e^{\lambda z}$, where $\lambda = \lambda_{1,2} = \pm\frac{1}{c_g}[\kappa^2 + (s + ik_x^2)^2]^{1/2}$. In this section $(\hat{E}_+, \hat{E}_-)^T$ denotes the solution of (2), i.e. the Fourier(x) + Laplace(t) transform of the solution of (1) ($\Gamma = 0$) for $z \in \{[-\delta_z, 0] \cup [L_z, L_z + \delta_z]\}$ and $(\hat{E}_+^{\text{pml}}, \hat{E}_-^{\text{pml}})$ stands for the transform of the solution of the to-be-determined PML equipped system on this domain.

The desired *absorption* in the z-layers will be satisfied if the following damping property in z holds when $-\delta_z \leqslant z < 0$ or $L_z < z \leqslant L_z + \delta_z$:

$$\begin{aligned} &\partial_z \hat{E}_\pm^{\text{pml}} = \tilde{\lambda} \hat{E}_\pm^{\text{pml}} \quad \text{with} \\ &\bullet\ \Re\tilde{\lambda} < 0 \text{ for right travelling modes and} \\ &\bullet\ \Re\tilde{\lambda} > 0 \text{ for left travelling modes,} \end{aligned} \tag{3}$$

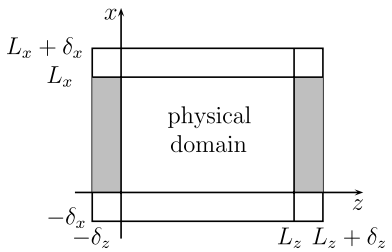

Fig. 2. Layers in the z-direction.

where right and left means in the positive and negative z-direction, respectively. As λ can be seen to satisfy the above conditions with $\leqslant$ and $\geqslant$, respectively, we simply need to ensure the strict nature of the inequalities. In order to also ensure that at the interfaces $z = 0$, L_z $(\hat{E}_+^{\mathrm{pml}}, \hat{E}_-^{\mathrm{pml}})$ *perfectly matches* the solution in the physical domain, we need

$$\lim_{z\to 0-}(\hat{E}_+^{\mathrm{pml}}, \hat{E}_-^{\mathrm{pml}}) = \lim_{z\to 0-}(\hat{E}_+, \hat{E}_-) \tag{4}$$

and similarly for $z \to L_z+$. Because of continuity of (E_+, E_-) across the interfaces this then gives continuity of the overall profile composed of $(E_+^{\mathrm{pml}}, E_-^{\mathrm{pml}})$ inside the layers and (E_+, E_-) in the physical domain.

Using the general approach of [5,16,18] for first order hyperbolic systems we give the following.

Proposition 1. *Replacing* λ *by* $\tilde{\lambda} = \frac{\lambda}{s+ik_x^2+\alpha}$ *with* $\alpha > 0$ *in* $(\hat{E}_+, \hat{E}_-)$ *yields* $(\hat{E}_+^{\mathrm{pml}}, \hat{E}_-^{\mathrm{pml}})$, *that satisfies the damping property* (3).

Proof. Let us study the two solution modes corresponding to $\lambda_{1,2} = \pm\frac{1}{c_g}[\kappa^2 + (s + ik_x^2)^2]^{1/2}$ separately.

(1) Because $\Re s \geqslant 0$, $k_x \in \mathbb{R}$ and c_g, $\kappa > 0$, it is easy to see that with the above described definition of the square root function Range(λ_1) is the right half of the complex plane excluding the upper half of the imaginary axis, i.e. Range$(\lambda_1) = \{re^{i\theta} | r \geqslant 0, -\pi/2 \leqslant \theta < \pi/2\}$. Therefore, λ_1 corresponds to left propagating modes.

To determine Range$(\tilde{\lambda}_1)$, i.e. the image of Range(λ_1) under the map $\lambda \to \tilde{\lambda}$, we first study the image of the lower half of the imaginary axis. Consider $\beta \geqslant 0$. At $\lambda = -i\beta$ it is $s + ik_x^2 + \alpha = (-c_g^2\beta^2 - \kappa^2)^{1/2} + \alpha = \alpha - i\sqrt{c_g^2\beta^2 + \kappa^2}$ and, therefore, division by $s + ik_x^2 + \alpha$ in the map $\lambda \to \tilde{\lambda}$ involves a rotation by the positive angle $-\phi = \arctan\left(\alpha^{-1}\sqrt{c_g^2\beta^2 + \kappa^2}\right) \in (0, \pi/2)$ which increases with β and attains the minimum value $-\phi^* = \arctan(\frac{\kappa}{\alpha})$ at $\beta = 0$.

Similarly, as λ approaches the upper half of the imaginary axis, i.e. for $\lambda_1 = \xi + i\beta$ with $\beta > 0$ and $\xi \to 0+$, one gets $s + ik_x^2 + \alpha \to \alpha + i\sqrt{c_g^2\beta^2 + \kappa^2}$ and the rotation is by the negative angle $\phi \in (-\pi/2, 0)$. Fig. 3 illustrates the rotation and shows a superset of Range$(\tilde{\lambda}_1)$.

(2) Analogously, $\lambda_2 = -\frac{1}{c_g}[\kappa^2 + (s + ik_x^2)^2]^{1/2}$ has Range$(\lambda_2) = \{re^{i\theta} | r \geqslant 0, \pi/2 \leqslant \theta < 3\pi/2\}$ and corresponds to right propagating modes. The rotations involved in the mapping $\lambda \to \tilde{\lambda}$ are exactly opposite to those for λ_1, see Fig. 4.

Using these facts one can easily check that the strict inequalities required in (3) are satisfied. Note that the origin, $\lambda = 0$, where $s = -ik_x^2 \pm i\kappa$, corresponds to waves propagating in the x-direction (so-called glancing waves), which are not required to be damped. □

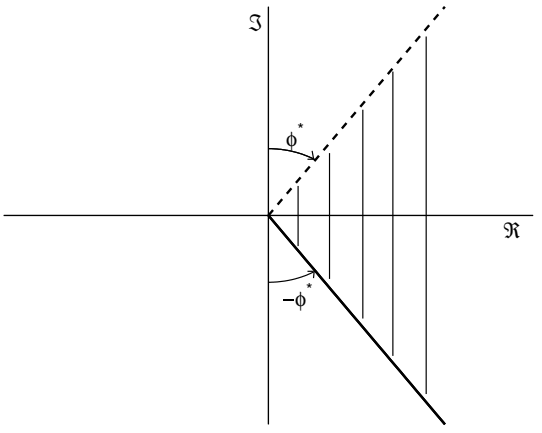

Fig. 3. A superset of Range$(\tilde{\lambda}_1)$.

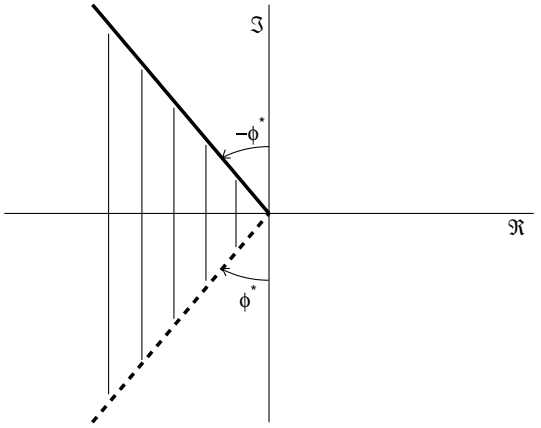

Fig. 4. A superset of Range($\tilde{\lambda}_2$).

The function $(\hat{E}_+^{\text{pml}}, \hat{E}_-^{\text{pml}}) = (c_1, c_2)\mathrm{e}^{\tilde{\lambda} z}$ does not, however, satisfy the perfect matching condition (4) as $\lim_{z\to L_z+}(\hat{E}_+^{\text{pml}}, \hat{E}_-^{\text{pml}}) = (c_1, c_2)\mathrm{e}^{\tilde{\lambda} L_z} \neq (c_1, c_2)\mathrm{e}^{\lambda L_z} = \lim_{z\to L_z+}(\hat{E}_+, \hat{E}_-)$. This can be easily remedied by replacing $\tilde{\lambda} z$ by $\lambda z + \tilde{\lambda}\int_{z_0}^{z} \sigma_z(\xi)\,\mathrm{d}\xi$ with $\sigma_z(\xi) \geqslant 0$ and $\int_{z_0}^{z} \sigma_z(\xi)\,\mathrm{d}\xi > 0$, where $z_0 = 0$ for $z < 0$ and $z_0 = L_z$ for $z > L_z$. The role of the integral and the function σ_z is for $(\hat{E}_+^{\text{pml}}, \hat{E}_-^{\text{pml}})$ to continuously deform into $(\hat{E}_+, \hat{E}_-)$ at the interface. σ_z can, moreover, be chosen to make the deformation arbitrarily smooth. The solution mode now becomes

$$\left(\hat{E}_+^{\text{pml}}, \hat{E}_-^{\text{pml}}\right) = (c_1, c_2)\mathrm{e}^{\lambda\left(z + \frac{\int_{z_0}^{z} \sigma_z(\xi)\,\mathrm{d}\xi}{s + \mathrm{i}k_x^2 + \alpha}\right)}. \tag{5}$$

In addition to the automatically satisfied perfect matching (4) the nth derivative in z is also matched if the $(n-1)$th derivative of σ_z converges to 0 at z_0. The constant in the damping property (3) is now $\lambda(1 + \frac{\sigma_z(z)}{s+\mathrm{i}k_x^2+\alpha})$ and one can easily check that its real part still satisfies the strict sign conditions, i.e. the direction of the rotation in Figs. 3 and 4 is preserved. For illustration, in Fig. 5 we show the mapping $\lambda_1 \to \lambda_1(1 + \frac{\sigma_z(z)}{s+\mathrm{i}k_x^2+\alpha})$ for λ_1 that lies on the negative imaginary axis.

In order to now derive the layer equations we study the relation between $\hat{E}_\pm$ and $\hat{E}_\pm^{\text{pml}}$:

$$\hat{E}_\pm = \hat{E}_\pm^{\text{pml}}\mathrm{e}^{\frac{-\lambda\int_{z_0}^{z} \sigma_z(\xi)\,\mathrm{d}\xi}{s+\mathrm{i}k_x^2+\alpha}}, \quad \partial_z\hat{E}_\pm = \left(\partial_z\hat{E}_\pm^{\text{pml}} - \frac{\lambda\sigma_z}{s+\mathrm{i}k_x^2+\alpha}\hat{E}_\pm^{\text{pml}}\right)\mathrm{e}^{\frac{-\lambda\int_{z_0}^{z} \sigma_z(\xi)\,\mathrm{d}\xi}{s+\mathrm{i}k_x^2+\alpha}}.$$

To account for the second term in $\partial_z\hat{E}_\pm$, we define auxiliary variables

$$\hat{F}_\pm := \mp c_{\mathrm{g}}\frac{\lambda\sigma_z(z)}{s+\mathrm{i}k_x^2+\alpha}\hat{E}_\pm^{\text{pml}}. \tag{6}$$

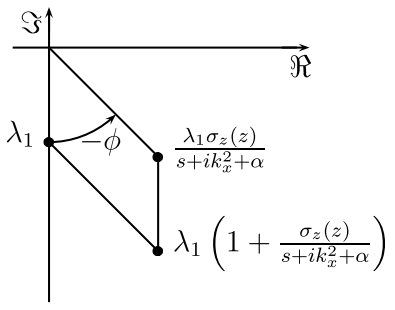

Fig. 5. Mapping of $\lambda_1 = -\mathrm{i}\beta$ as in the solution (5).

The *layer equations*, i.e. equations satisfied by $(E_+^{\mathrm{pml}}, F_+, E_-^{\mathrm{pml}}, F_-)^T$, then read

$$\begin{aligned}
&\mathrm{i}(\partial_t E_+ + c_g \partial_z E_+ + F_+) + \kappa E_- + \partial_x^2 E_+ = 0,\\
&\partial_t F_+ + c_g \sigma_z \partial_z E_+ - i\partial_x^2 F_+ + (\alpha + \sigma_z) F_+ = 0,\\
&\mathrm{i}(\partial_t E_- - c_g \partial_z E_- + F_-) + \kappa E_+ + \partial_x^2 E_- = 0,\\
&\partial_t F_- - c_g \sigma_z \partial_z E_- - i\partial_x^2 F_- + (\alpha + \sigma_z) F_- = 0
\end{aligned} \tag{7}$$

with $F_\pm(t=0) \equiv 0$.

The second and fourth equations in (7) are obtained by relating $\hat{F}_\pm$ with $\partial_z \hat{E}_\pm^{\mathrm{pml}}$. From (5) one has

$$\hat{E}_\pm^{\mathrm{pml}} = \frac{s + \mathrm{i}k_x^2 + \alpha}{\lambda(s + \mathrm{i}k_x^2 + \alpha + \sigma_z)} \partial_z \hat{E}_\pm^{\mathrm{pml}}.$$

Thus, using (6),

$$(s + \mathrm{i}k_x^2 + \alpha + \sigma_z)\hat{F}_\pm = \mp c_g \sigma_z \partial_z \hat{E}_\pm^{\mathrm{pml}},$$

which is equivalent to the second and fourth equations in (7), respectively.

For the *1D coupled mode equations* the derivation of layer equations is completely analogous to the previous discussion (with $k_x = 0$) and leads to

$$\begin{aligned}
&\mathrm{i}(\partial_t E_+ + c_g \partial_z E_+ + F_+) + \kappa E_- = 0,\\
&\partial_t F_+ + c_g \sigma_z \partial_z E_+ + (\alpha + \sigma_z) F_+ = 0,\\
&\mathrm{i}(\partial_t E_- - c_g \partial_z E_- + F_-) + \kappa E_+ = 0,\\
&\partial_t F_- - c_g \sigma_z \partial_z E_- + (\alpha + \sigma_z) F_- = 0
\end{aligned} \tag{8}$$

with $E_\pm = E_\pm(z,t)$ and $F_\pm = F_\pm(z,t)$.

4. *x*-Layer equations

The dynamics of the linear part of (1) ($\Gamma = 0$) in the x-direction are similar to those of the linear Schrödinger equation (LSE) and, therefore, the layer equations in the x-layers $[-\delta_x, 0]\times[0, L_z]$ and $[L_x, L_x + \delta_x]\times[0, L_z]$, see Fig. 6, turn out to be analogous to those of the LSE [12,18]. After the Laplace–Fourier transform in (t, z) the linear part of (1) becomes for $x < 0$ or $x > L_x$

$$\begin{aligned}
&(\mathrm{i}s - c_g k_z)\hat{E}_+ + \kappa \hat{E}_- + \partial_x^2 \hat{E}_+ = 0,\\
&(\mathrm{i}s + c_g k_z)\hat{E}_- + \kappa \hat{E}_+ + \partial_x^2 \hat{E}_- = 0
\end{aligned} \tag{9}$$

with solution modes $(\hat{E}_+, \hat{E}_-) = (c_1, c_2)\mathrm{e}^{\lambda x}$, where $\lambda = \lambda_{1,2} = \pm[-\mathrm{i}s \pm \sqrt{c_g^2 k_z^2 + \kappa^2}]^{1/2}$. Analogously to (3) we seek a solution $(\hat{E}_+^{\mathrm{pml}}, \hat{E}_-^{\mathrm{pml}})$ such that when $-\delta_x \leqslant x < 0$ or $L_x < x \leqslant L_x + \delta_x$,

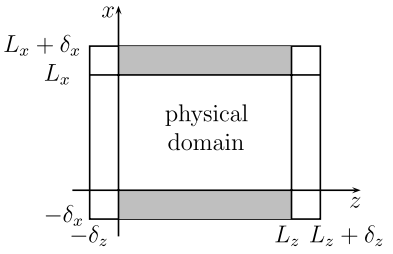

Fig. 6. Layers in the x-direction.

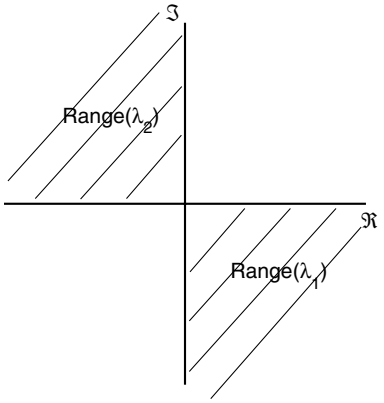

Fig. 7. Range($\lambda_{1,2}$).

$\partial_x \hat{E}_{\pm}^{\mathrm{pml}} = \tilde{\lambda}\hat{E}_{\pm}^{\mathrm{pml}}$ with

- $\Re\tilde{\lambda} < 0$ for up travelling modes and
- $\Re\tilde{\lambda} > 0$ for down travelling modes, (10)

where up and down means in the positive and negative x-direction, respectively. Similar to Section 3 ($\hat{E}_+, \hat{E}_-$) is the Fourier(x) + Laplace(t) transform of the solution of (1) ($\Gamma = 0$) for $x \in \{[-\delta_x, 0] \cup [L_x, L_x + \delta_x]\}$ and ($\hat{E}_+^{\mathrm{pml}}, \hat{E}_-^{\mathrm{pml}}$) is the transform of the PML equipped system.

Since $\Re s \geqslant 0$, it is easy to see that Range(λ_1) $= \{re^{i\theta} | r \geqslant 0, -\pi/2 \leqslant \theta \leqslant 0\}$, see Fig. 7. $\lambda_{1,2}$ correspond to up and down propagating modes respectively since otherwise the modes would not be bounded. Because their ranges are only quadrants (as opposed to the half planes in the z-layer case), a simple rotation $\tilde{\lambda} = e^{i\rho}\lambda, \rho \in (0, \pi/2)$ would ensure the strict inequalities in (10). In order to also achieve perfect matching, we let

$$\left(\hat{E}_+^{\mathrm{pml}}, \hat{E}_-^{\mathrm{pml}}\right) = (c_1, c_2) e^{\lambda\left(x + e^{i\rho}\int_{x_0}^{x} \sigma_x(\xi)\, d\xi\right)} \tag{11}$$

with $x_0 = 0$ for $x < 0$ and $x_0 = L_x$ for $x > L_x$, $\rho \in (0, \pi/2)$ and σ_x defined analogously to σ_z. We note, however, that due to the presence of second x-derivatives perfect matching also requires besides the condition (4) continuity of the first x-derivatives. This is accomplished by imposing the additional condition

$$\sigma_x(x_0) = 0. \tag{12}$$

Since

$$E_{\pm} = E_{\pm}^{\mathrm{pml}} e^{-\lambda e^{i\rho}\int_{x_0}^{x} \sigma_x(\xi)\, d\xi} \quad \text{and} \quad \partial_x E_{\pm} = \frac{1}{1 + \sigma_x e^{i\rho}} \partial_x E_{\pm}^{\mathrm{pml}} e^{-\lambda e^{i\rho}\int_{x_0}^{x} \sigma_x(\xi)\, d\xi},$$

the layer equations become

$$i(\partial_t E_{\pm} \pm c_g \partial_z E_{\pm}) + \kappa E_{\mp} + \frac{1}{1 + \sigma_x e^{i\rho}} \partial_x \left(\frac{1}{1 + \sigma_x e^{i\rho}} \partial_x E_{\pm} \right) = 0. \tag{13}$$

5. Equations in the corner layers

The most natural treatment of the corner layers $[-\delta_x, 0] \times [-\delta_z, 0]$, $[-\delta_x, 0] \times [L_z, L_z + \delta_z]$, $[L_x, L_x + \delta_x] \times [-\delta_z, 0]$ and $[L_x, L_x + \delta_x] \times [L_z, L_z + \delta_z]$ is, of course, to extend and combine Eqs. (7) and (13) to these regions (see Fig. 8). This results in

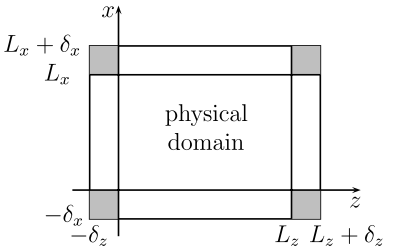

Fig. 8. Corner layers.

$$
\begin{aligned}
&\mathrm{i}(\partial_t E_+ + c_g \partial_z E_+ + F_+) + \kappa E_- + \frac{1}{1+\sigma_x \mathrm{e}^{\mathrm{i}\rho}} \partial_x \left(\frac{1}{1+\sigma_x \mathrm{e}^{\mathrm{i}\rho}} \partial_x E_+ \right) = 0,\\
&\partial_t F_+ + c_g \sigma_z \partial_z E_+ - \mathrm{i} \frac{1}{1+\sigma_x \mathrm{e}^{\mathrm{i}\rho}} \partial_x \left(\frac{1}{1+\sigma_x \mathrm{e}^{\mathrm{i}\rho}} \partial_x F_+ \right) + (\alpha + \sigma_z) F_+ = 0,\\
&\mathrm{i}(\partial_t E_- - c_g \partial_z E_- + F_-) + \kappa E_+ + \frac{1}{1+\sigma_x \mathrm{e}^{\mathrm{i}\rho}} \partial_x \left(\frac{1}{1+\sigma_x \mathrm{e}^{\mathrm{i}\rho}} \partial_x E_- \right) = 0,\\
&\partial_t F_- - c_g \sigma_z \partial_z E_- - \mathrm{i} \frac{1}{1+\sigma_x \mathrm{e}^{\mathrm{i}\rho}} \partial_x \left(\frac{1}{1+\sigma_x \mathrm{e}^{\mathrm{i}\rho}} \partial_x F_- \right) + (\alpha + \sigma_z) F_- = 0.
\end{aligned}
\tag{14}
$$

Replacing ∂_x^2 by $\frac{1}{1+\sigma_x \mathrm{e}^{\mathrm{i}\rho}} \partial_x \left(\frac{1}{1+\sigma_x \mathrm{e}^{\mathrm{i}\rho}} \partial_x \right)$ in the equations for the auxiliary functions $F_\pm$ ensures consistency of the PML formulation, i.e. the rotation involved in $\lambda \to \tilde{\lambda}$ is now the same throughout each of the z-layers $[-\delta_x, L_x + \delta_x] \times [-\delta_z, 0]$ and $[-\delta_x, L_x + \delta_x] \times [L_z, L_z + \delta_z]$. The same analysis as in Section 3 can be used (with constant σ_x) to show that the z-damping property and perfect matching in z are satisfied for Eqs. 14. Performing the analysis, one now obtains the linear mode $(\hat{E}_+^{\mathrm{pml}}, \hat{E}_-^{\mathrm{pml}}) = (c_1, c_2) \mathrm{e}^{\lambda \left(z + (s + \mathrm{i}\mu^2 k_x^2 + \alpha)^{-1} \int_{z_0}^{z} \sigma_z(\xi)\, \mathrm{d}\xi \right)}$, where $\lambda = \pm \frac{1}{c_g} [\kappa^2 + (s + \mathrm{i}\mu^2 k_x^2)^2]^{1/2}$ and $\mu = (1 + \sigma_x \mathrm{e}^{\mathrm{i}\rho})^{-1}$, cf. Eq. (5). It is not obvious how to analytically prove the damping and perfect matching in x but the numerical tests presented below suggest this to be satisfied also.

In Section 7 we use the above derived PML equations even in the nonlinear regime under the assumption of $|E_+|$ and $|E_-|$ being small in the layers. The governing system is then (14) with the addition of $\Gamma(|E_+|^2 + 2|E_-|^2)E_+$ and $\Gamma(|E_-|^2 + 2|E_+|^2)E_-$ to the left-hand side of the first and third equations, respectively. One analogously "delinearizes" the 1D system (8).

6. Stability of the layer equations

We now follow the analysis in [5] to establish the stability of the corner layer system (14) assuming constant layer parameters. We realize that to maintain perfect matching one must use varying values of σ_x, but nonetheless we believe the following result with constant σ_x provides complementary evidence to the numerical experiments that the layer equations are stable. They do establish that the layer equations are well-posed. The analysis, which is based on the Sturm sequence method for bounding the roots of polynomial equations, also can be used to derive energy estimates; see [19] for details.

Performing a Fourier transformation in (x, z) and solving for time derivatives leads to a system:

$$
\frac{\mathrm{d}\hat{W}}{\mathrm{d}t} = -\mathrm{i} \frac{k_x^2}{(1+\sigma_x \mathrm{e}^{\mathrm{i}\rho})^2} \hat{W} + \hat{P}\hat{W}, \tag{15}
$$

where $\hat{W} = (\hat{E}_+, \hat{F}_+, \hat{E}_-, \hat{F}_-)^{\mathrm{T}}$. We will prove that if $\sigma_z > 0$ and $\alpha > 0$, then the eigenvalues of the 4×4 matrix $\hat{P}$ have negative real part (unless $k_z = 0$). Since

$$
\Re \left(-\mathrm{i} \frac{k_x^2}{(1+\sigma_x \mathrm{e}^{\mathrm{i}\rho})^2} \right) = -\frac{\sigma_x k_x^2}{(1+\sigma_x^2)^2} (2 \sin \rho + \sigma_x \sin 2\rho), \tag{16}
$$

we will have proven stability under the additional assumptions $\sigma_x > 0$, $0 < \rho < \frac{\pi}{2}$.

To establish the result concerning the eigenvalues of $\hat{P}$, we compute its characteristic polynomial:

$$\lambda^4 + a\lambda^3 + b\lambda^2 + c\lambda + d, \tag{17}$$

$$\begin{aligned} a &= 2(\alpha + \sigma_z), \\ b &= (\alpha + \sigma_z)^2 + c_g^2 k_z^2 + \kappa^2, \\ c &= 2(\alpha c_g^2 k_z^2 + (\alpha + \sigma_z)\kappa^2), \\ d &= \alpha^2 c_g^2 k_z^2 + (\alpha + \sigma_z)^2 \kappa^2. \end{aligned} \tag{18}$$

Application of the Sturm sequence technique yields that the roots have negative real parts if and only if

$$\begin{aligned} &a > 0, \\ &ab - c > 0, \\ &c(ab - c) - a^2 d > 0, \\ &d > 0. \end{aligned} \tag{19}$$

Carrying through the algebra one easily checks that these inequalities hold so long as $\alpha > 0$, $\sigma_z > 0$, and $c_g k_z \neq 0$. We note that if $c_g k_z = 0$ the system has two distinct imaginary roots and thus is neutrally stable for such modes. Note that the neutrally stable $k_z = 0$ modes have zero group velocity and cannot propagate into the layer.

Stability of the layer equations (7) and (13) follows from the above result.

7. Numerical experiments

We perform numerical finite difference (FD) time domain simulations of the 1D and 2D CME in both linear ($\Gamma = 0$) and nonlinear ($\Gamma > 0$) regimes and study the performance of the PML. It can be shown that taking the absorbing layer of a finite width generates reflections from the boundary $z = -\delta_z$, $L_z + \delta_z$ (or $x = -\delta_x$, $L_x + \delta_x$), which decrease exponentially as the layer width is increased, i.e. like $e^{-p\delta_z}$ (or $e^{-p\delta_x}$) with $p > 0$ [8,9,16,24]. We show this *exponential error convergence* to be true for the above constructed PML for 1D and 2D linear CME and show that a decreased exponential rate can be obtained *even in the nonlinear case*. The convergence rate is decreased most dramatically when, in the nonlinear regime, a disturbance with a relatively large amplitude (so that $|E_\pm|^2 E_\pm$ is non-negligible) enters a PML layer. In such cases one should, actually, expect even a failure of the absorption and lack of error convergence. In the cases presented here this is not, however, the case. It is, nevertheless, the satisfactory behavior in situations when the solution is only weakly nonlinear in the layers (main pulse stays in the physical domain) that is more important in typical nonlinear optics simulations, see Section 1.

7.1. 1D CME tests

1D CME with PML are given by (8), where $F_\pm$ are only defined inside the layers $[-\delta_z, 0]$, $[L_z, L_z + \delta_z]$. We use the following third order upwind FD formula for ∂_z, $\partial_z u(z_i) \approx (-3u_{i-1} - 10u_i + 18u_{i+1} - 6u_{i+2} + u_{i+3})/(12\,\mathrm{d}z)$, where $u_i = u(z_i)$. This formula is used 'verbatim' in the E_- equation while the direction of upwinding is reversed for the E_+ equation. The layers are terminated via the zero Dirichlet boundary condition $E_\pm(-\delta_z, t) = E_\pm(L_z + \delta_z, t) = F_\pm(-\delta_z, t) = F_\pm(L_z + \delta_z, t) = 0$.

The PML parameter α is chosen $\alpha = 2$ and we take a smooth profile of the function $\sigma_z(z)$, namely

$$\sigma_z(z) = \begin{cases} h_z[1 + \tanh(a_z(\delta_z)(z - L_z - \delta_z/2))] & \text{if } L_z \leqslant z \leqslant L_z + \delta_z, \\ h_z[1 - \tanh(a_z(\delta_z)(z + \delta_z/2))] & \text{if } -\delta_z \leqslant z < 0 \end{cases} \tag{20}$$

with a_z, $h_z > 0$. The slope parameter $a_z = a_z(\delta_z)$ is taken inversely proportional to δ_z so that σ_z 'stretches' with increasing δ_z. As our tests have shown, this results in higher convergence rates of the error as a function of δ_z than if the shape of σ_z does not change with δ_z. Finally, the PDE coefficients c_g and κ are fixed at $c_g = \kappa = 1$.

7.1.1. Linear evolution ($\Gamma = 0$)

In this test we take $\Gamma = 0$, $L_z = 8$, $dz = 0.001$ and the Gaussian initial data $E_+(z,0) = E_-(z,0) = e^{-(z-L_z/2)^2}$. Setting the amplitude parameter of σ_z to $h_z = 100$ and the slope parameter to $a_z = 24/\delta_z$, we study the error convergence with respect to δ_z, taking $\delta_z = 0.6$, 0.9, 1.2 and 1.5.

The linear dynamics always lead to E_+ and E_- propagating in opposite directions according to the linear advection part of the equations. We present results for three different points in time; $t = 4$ (Figs. 9 and 10) when only radiation but not the main pulses in E_+ and E_- have reached the layers, $t = 6$ (Figs. 11 and 12) when a large part of the pulses has entered the PML layers and, in order to also check long time properties of the PML, $t = 20$ (Figs. 13 and 14) when almost all energy has left the physical domain. The error is computed with respect to the exact solution obtained by applying the solution operator of the linear PDE

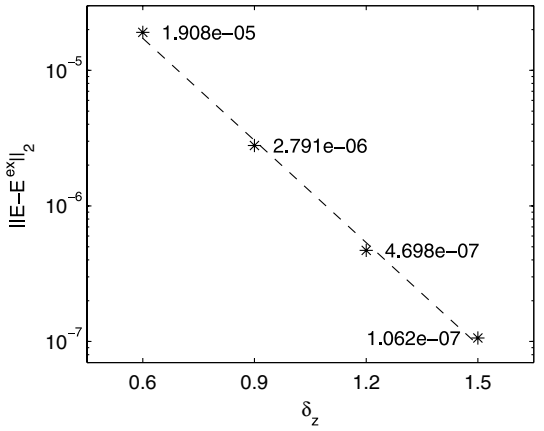

Fig. 9. Error convergence. ∗, L^2 error at $t = 4$; ––, $ce^{-5.79\delta_z}$.

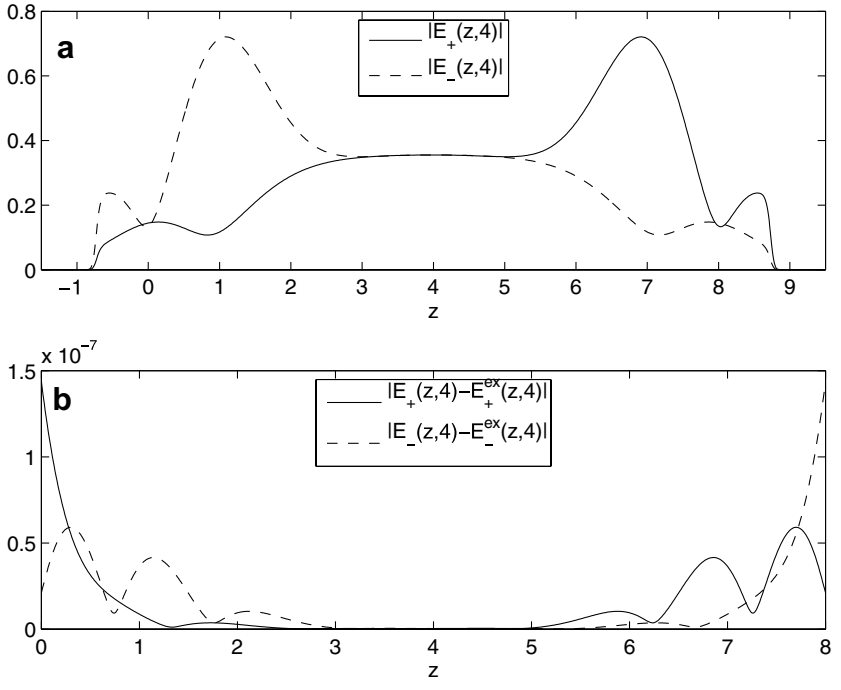

Fig. 10. (a) Solution modulus and (b) error at $t = 4$ for $\delta_z = 1.5$.

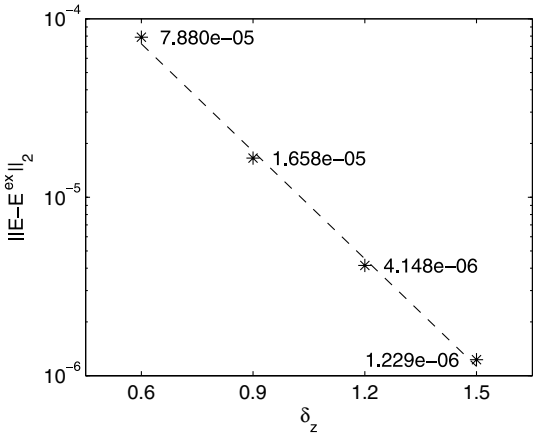

Fig. 11. Error convergence. ∗, L^2 error at $t = 6$; ––, $ce^{-4.62\delta_z}$.

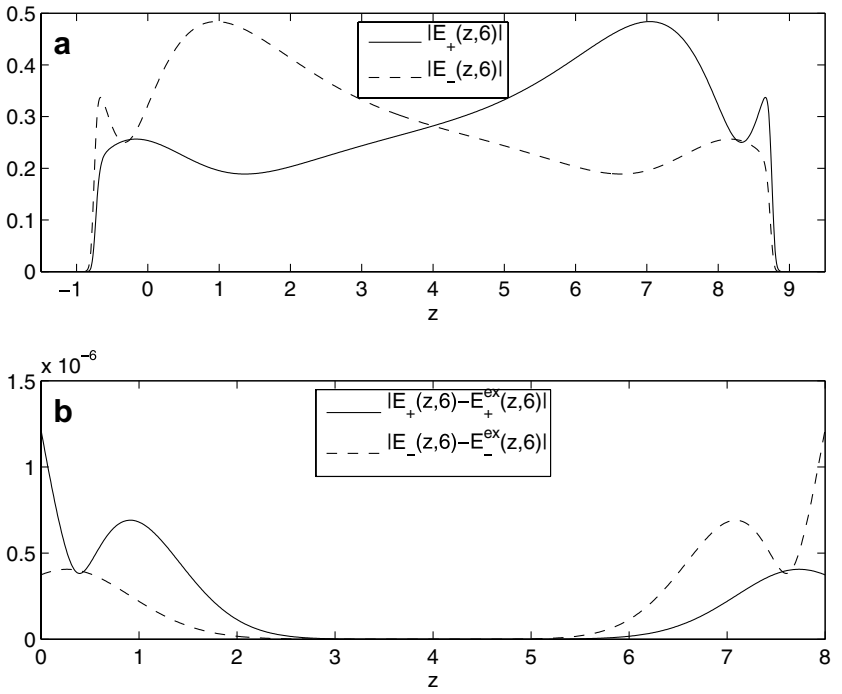

Fig. 12. (a) Solution modulus and (b) error at $t = 6$ for $\delta_z = 1.5$.

in Fourier space on a physical domain that is large enough so that the solution remains well decayed at the boundary, namely on $[-2L_z, 3L_z - \mathrm{d}z]$. The resulting convergence and error values in the L^2 norm are shown. Figs. 9, 11 and 13 show that the obtained error convergence is exponential with approximate rates 5.8, 4.6 and 3.6. (Note that a decrease in the exponent with increasing time is predicted by the analysis in [8,9,16].) Figs. 10, 12 and 14 show the modulus of both components E_+ and E_- on the whole domain including the PML layers for the case of the widest layer and the corresponding error inside the physical domain. The error plots clearly show that the error is initially concentrated near the physical domain boundaries, which is due to the reflections induced by truncating the layers to a finite width.

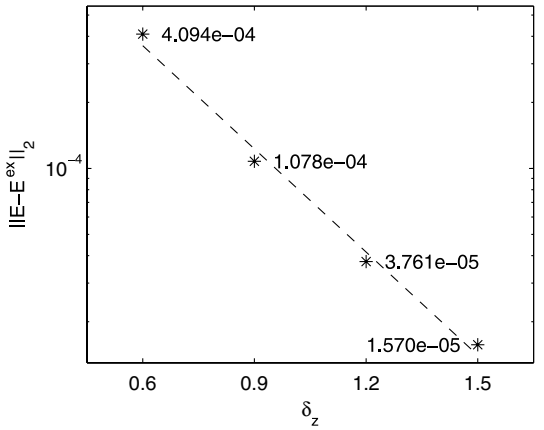

Fig. 13. Error convergence. $*$, L^2 error at $t = 20$; $--$, $ce^{-3.61\delta_z}$.

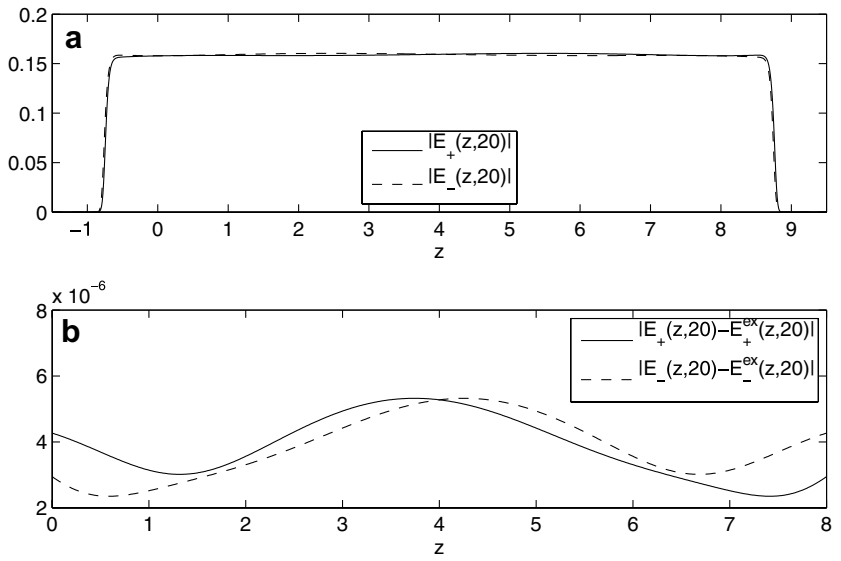

Fig. 14. (a) Solution modulus and (b) error at $t = 20$ for $\delta_z = 1.5$.

7.1.2. Nonlinear evolution

When $\Gamma > 0$, the 1D model without PML (Eq. (1) with $\partial_x^2 = 0$) has a family of closed form solitary wave solutions, so-called gap solitons [2,7]. These are localized pulses parameterized by the velocity $v \in (-c_g, c_g)$ and a detuning parameter $\delta \in (0, \pi)$:

$$E_\pm = \pm\alpha e^{i\eta}\sqrt{\frac{\kappa}{2\Gamma}}\sin(\delta)\Delta^{\mp 1}e^{i\sigma}sech(\theta \mp i\delta/2), \tag{21}$$

where

$$\alpha = \sqrt{\frac{2(1-v^2)}{3-v^2}}, \quad \Delta = \left(\frac{1-v}{1+v}\right)^{1/4}, \quad \theta = \gamma\kappa\sin(\delta)\left(\frac{z-z_0}{c_g} - vt\right), \quad \sigma = \gamma\kappa\cos(\delta)\left(\frac{v}{c_g}(z-z_0) - t\right),$$

$$\gamma = (1-v^2)^{-1/2}, \quad e^{i\eta} = \left(-\frac{e^{2\theta}+e^{-i\delta}}{e^{2\theta}+e^{i\delta}}\right)^{\frac{2v}{3-v^2}} = e^{i\frac{4v}{3-v^2}\arctan\left(\frac{e^{2\theta}+\cos(\delta)}{\sin(\delta)}\right)}.$$

Both $|E_+|$ and $|E_-|$ are the hyperbolic secant function and they propagate in the same direction. We use these special solutions for the following test. Since the gap solitons are not true solitons in the sense of the inverse scattering transform, they do not interact elastically with each other. Collisions of two gap solitons generally result in large amounts of radiation. We simulate such a collision of two relatively slow ($|v| = 0.3$) gap solitons and study radiation absorption by the PML, see Fig. 15. The radiation travels at the group velocity c_g, i.e. much faster than the gap solitons. Because of the small speed of the gap solitons we can study relatively long time dynamics ($t = 30$) with only small amplitude waves reaching the PML layers. We also investigate the PML performance at an even larger time ($t = 40$) when one of the gap solitons has itself entered the layer.

The chosen parameters are $\Gamma = 1$, $L_z = 24$ and $\mathrm{d}z = 0.03$ and the initial data are

$$\begin{pmatrix} E_+(z,0) \\ E_-(z,0) \end{pmatrix} = GS_A(z) + GS_B(z),$$

where GS_A is the gap soliton (21) with $t = 0$, $v = 0.3$, $\delta = \pi/2$ and $z_0 = L_z/4$ and GS_B is (21) with $t = 0$, $v = -0.3$, $\delta = \pi/2$ and $z_0 = 3L_z/4$, see Fig. 15a. Four different layer widths are considered: $\delta_z = 0.6$, 0.9, 1.2 and 1.5. The amplitude parameter of the function σ_z is $h_z = 60$ and the slope parameter is $a_z(\delta_z) = 18/\delta_z$.

Figs. 16 and 17 present the results at $t = 30$, when both pulses are still inside the physical domain but have already collided and Figs. 18 and 19 are for $t = 40$, when one of the pulses has completely entered the layer.

The error (L^2) convergence appears to be still exponential with the rate $p \approx 0.8$ at $t = 30$ and $p \approx 0.1$ at $t = 40$. Of course, the error is greatly increased in the latter case near the layer which the large disturbance has reached. This is not unexpected as the PML is designed to work only for linear dynamics. The satisfactory performance for radiation absorption ($t = 30$) is, nevertheless, very encouraging as that is the main purpose of PML in nonlinear optics simulations.

7.2. 2D CME tests

We now turn to the full 2D system (14) on the physical domain $(x, z) \in [0, L_x] \times [0, L_z]$ appended with the PML layers of width δ_x and δ_z in x and z, respectively, see Fig. 1. Recall that F_+ and F_- need to be defined

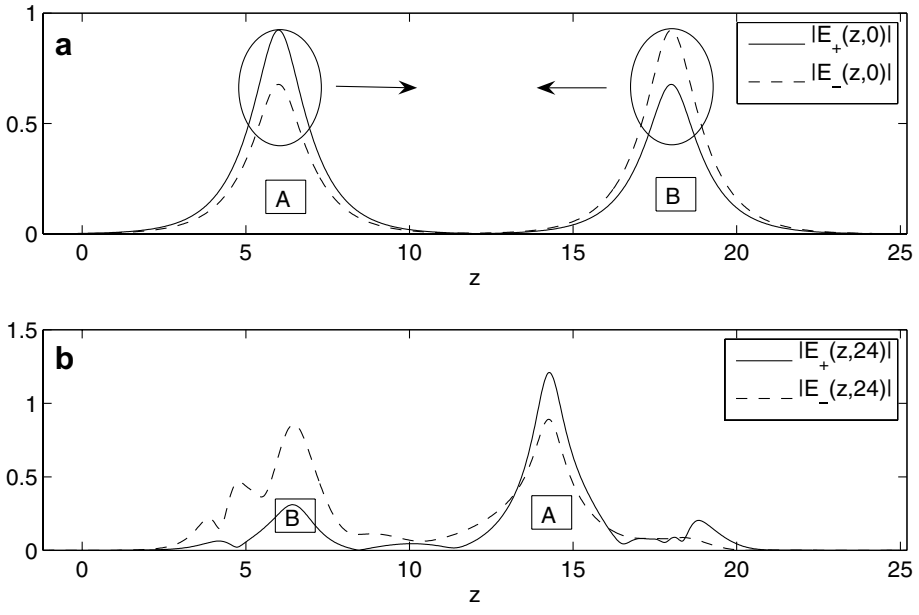

Fig. 15. (a) Modulus of initial data and (b) after interaction at $t = 24$.

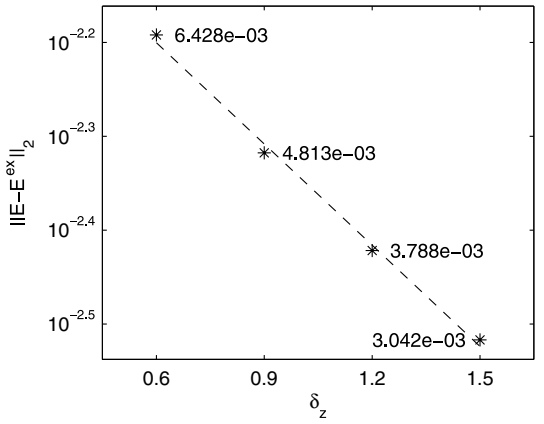

Fig. 16. Error convergence. $*$, L^2 error at $t = 30$; $--$, $ce^{-0.83\delta_z}$.

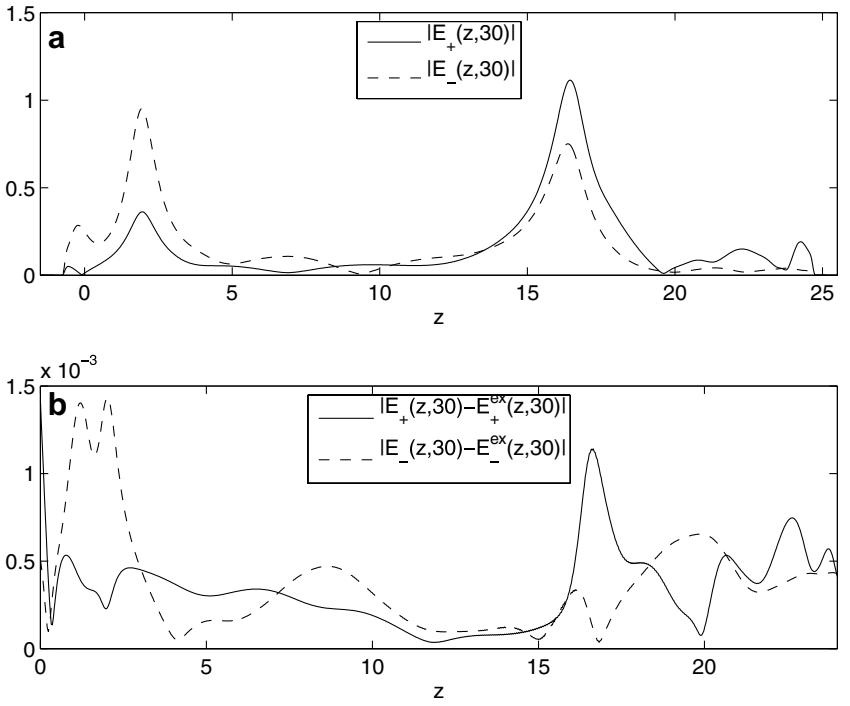

Fig. 17. (a) Solution modulus and (b) error at $t = 30$ for $\delta_z = 1.5$.

only inside the z-layers $[-\delta_x, L_x + \delta_x]\times[-\delta_z, 0]$ and $[-\delta_x, L_x + \delta_x]\times[L_z, L_z + \delta_z]$, which is what we also do in our FD implementation. The FD approximation of ∂_z is done using the same upwind formulas as in Section 7.1 and ∂_x^2 is approximated via the third order central difference formula $\partial_x^2 u(x_i, z_j) \approx (-u_{i-2,j} + 16u_{i-1,j} - 30u_{i,j} + 16u_{i+1,j} - u_{i+2,j})/(12dx^2)$, where $u_{i,j} = u(x_i, z_j)$. As in the 1D case, we use zero Dirichlet boundary conditions on $E_\pm$ as well as $F_\pm$ at the layer ends $z = -\delta_z, L_z + \delta_z$ and $x = -\delta_x, L_x + \delta_x$. Time evolution is treated by a fourth order additive Runge–Kutta scheme of the ESDIRK type [21] which allows us to treat the second derivative (stiff) terms implicitly and the remaining terms explicitly leading to a first order

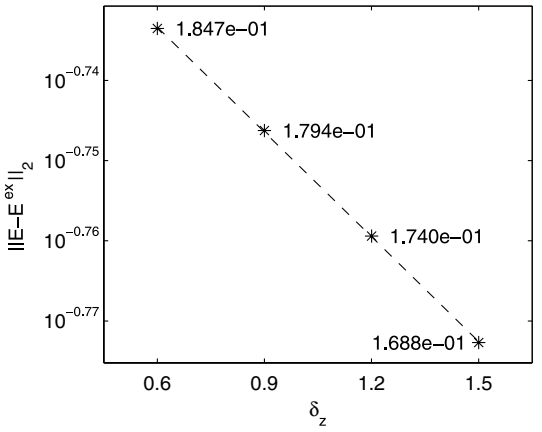

Fig. 18. Error convergence. ∗, L^2 error at $t = 40$; ––, $ce^{-0.1\delta_z}$.

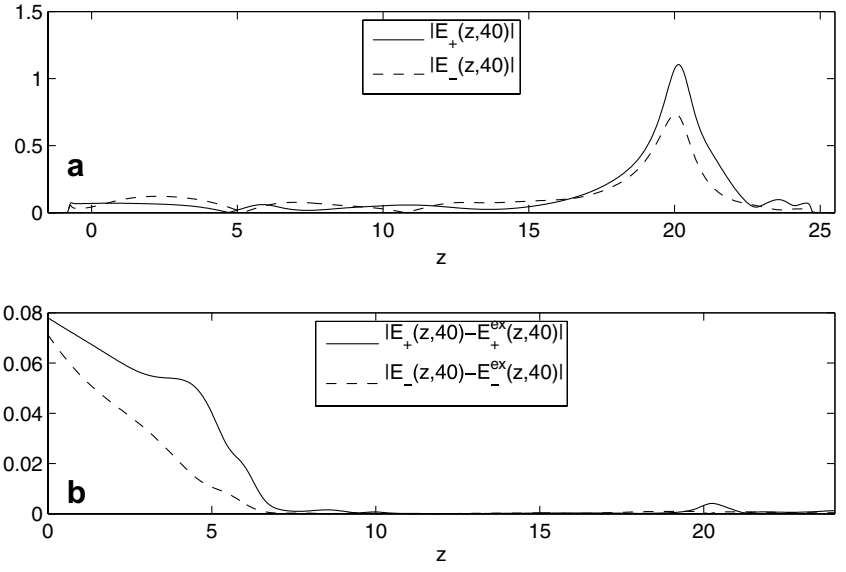

Fig. 19. (a) Solution modulus and (b) error at $t = 40$ for $\delta_z = 1.5$.

CFL condition. We only need to solve $2(Nz + 2Nz_{\text{pml}})$[1] linear systems of size $N_x \times N_x$ at each stage of the Runge–Kutta method because the implicitly treated part has only x-derivative terms and no coupling between E_+ and E_-.

The PML parameters are chosen $\alpha = 1$, $\rho = \pi/4$, the function σ_z is given in (20), σ_x is completely analogous (replace all z by x) and we fix $h_z = h_x = 40$. Also, once again, the PDE coefficients are $\kappa = c_g = 1$.

7.2.1. Linear evolution

We take $\Gamma = 0$, $L_z = 1$, $L_x = 2$, $\mathrm{d}z = 0.01$, $\mathrm{d}x = 0.02$ and $\mathrm{d}t = 0.001$ and the Gaussian initial data $E_+(x,z,0) = E_-(x,z,0) = \mathrm{e}^{-30(x-L_x/2)^2-40(z-L_z/2)^2}$. Setting the slope parameters of σ_z and σ_x to $a_z = 8/\delta_z$ and $a_x = 12/\delta_x$, we study the error convergence with respect to δ_x and δ_z, taking $\delta_x = 2\delta_z = 0.4$, 0.5, 0.6, 0.7 and 0.8.

Similarly to the 1D case the linear dynamics lead to transport of energy in both the positive and negative z-directions but more dominant is the diffraction (spreading) in the x-direction. We present results of

[1] $Nz_{\text{pml}} = \delta_z/\mathrm{d}z$ is the number of computational points across the z-width of each PML z-layer.

simulations at $t = 0.6$ shortly after the main pulses have entered the z-layers. At this time, however, the fast x-diffraction has already resulted in a very wide (in x) solution causing a large portion of the initial energy to be absorbed by the x-layers. This also forces us to use a wide domain, namely $(x, z) \in [-70L_x, 71L_x] \times [-L_z, 2L_z]$ for the application of the solution operator in Fourier space in order to find the 'exact' solution for error computations. We also present results at $t = 6$ to study 'long' time performance of the PML.

The results at $t = 0.6$ for the widest layers are presented in Figs. 21 and 22. The convergence is exponential with an approximate rate $p \approx 7.3$, see Fig. 20, and one can clearly see in Fig. 22 that the error is concentrated near $z = L_z$ for E_+ and near $z = 0$ for E_-, which is due to the artificial reflections caused by layer truncation. x-symmetric error due to reflections from the x-layer boundaries is, however, also apparent.

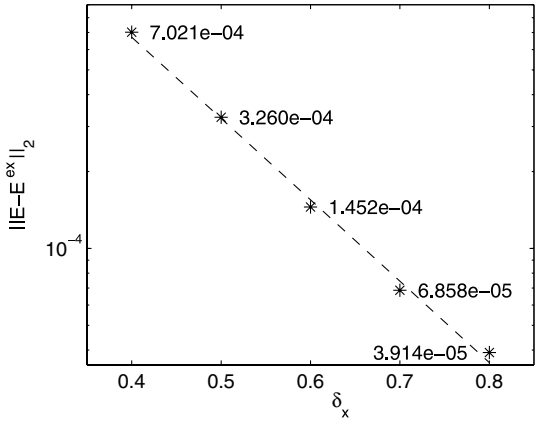

Fig. 20. Error convergence. ∗, L^2 error at $t = 0.6$; ––, $ce^{-7.33\delta_x}$.

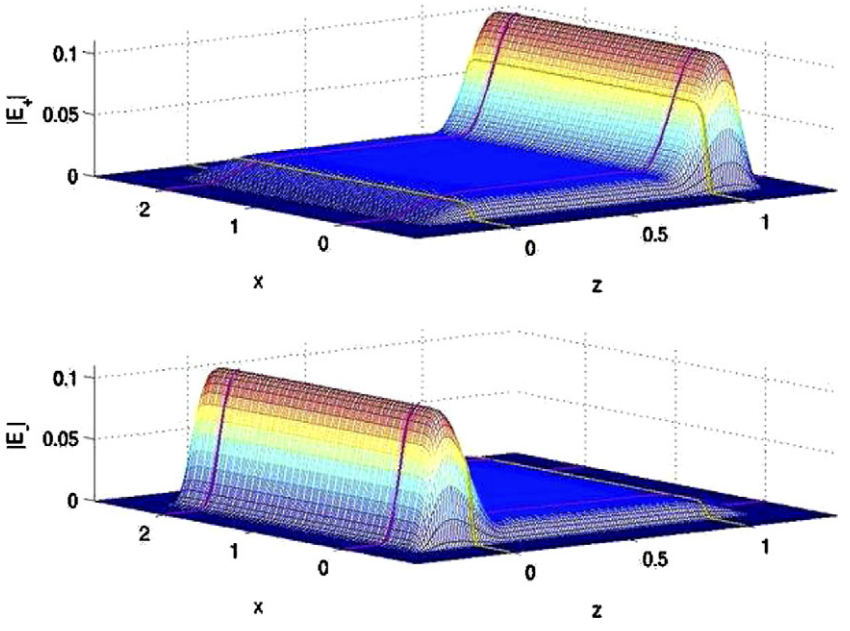

Fig. 21. Solution modulus at $t = 0.6$ for $\delta_x = 2\delta_z = 0.8$.

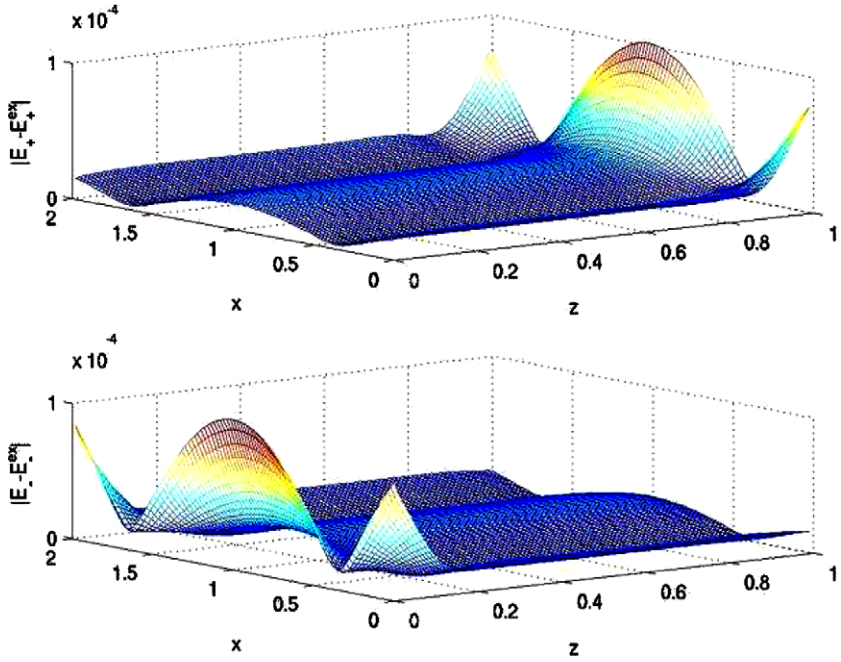

Fig. 22. Error at $t = 0.6$ for $\delta_x = 2\delta_z = 0.8$.

For the long time behavior the solution modulus at $t = 6$ is shown in Fig. 23. Using differences of solutions computed with different layer widths we estimate the convergence rate. For exponential rate, when error $= ce^{-p\delta_x}$, one has

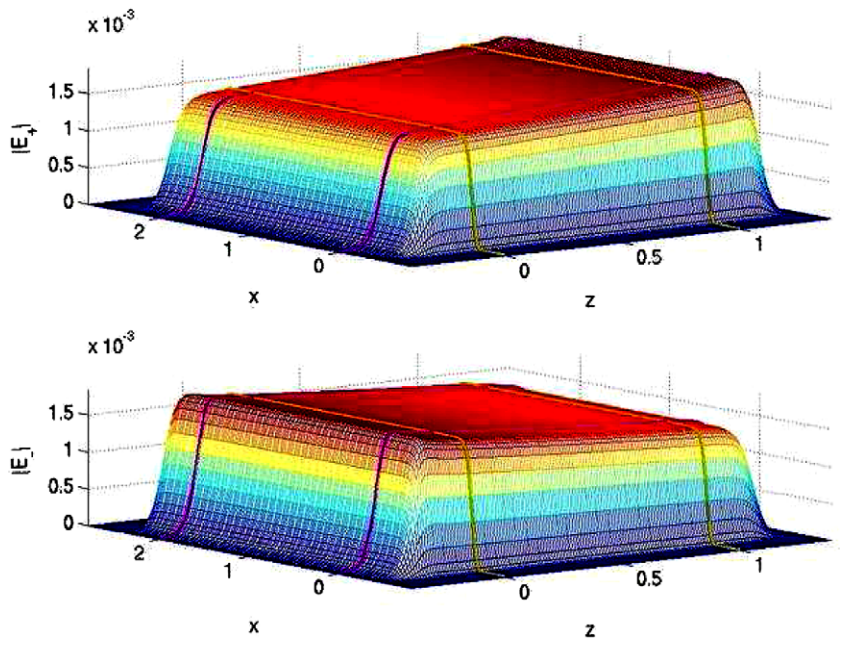

Fig. 23. Solution modulus at $t = 6$ for $\delta_x = 2\delta_z = 0.8$.

$$\frac{\|\vec{E}^{(1)} - \vec{E}^{(2)}\|}{\|\vec{E}^{(1)} - \vec{E}^{(3)}\|} = \frac{1 - e^{-p(\delta_x^{(2)} - \delta_x^{(1)})}}{1 - e^{-p(\delta_x^{(3)} - \delta_x^{(1)})}}. \tag{22}$$

We choose $\vec{E}^{(1)}$, $\vec{E}^{(2)}$ and $\vec{E}^{(3)}$ to be the solutions $(E_+, E_-)^T$ corresponding to the three widest layers $\delta_x^{(1)} = 2\delta_z^{(1)} = 0.6$, $\delta_x^{(2)} = 2\delta_z^{(2)} = 0.7$ and $\delta_x^{(3)} = 2\delta_z^{(3)} = 0.8$, respectively. The norms on the left-hand side of (22) are L^2 norms over the physical domain $[0, L_x] \times [0, L_z]$. Solving (22) in p via Newton's iteration results in $p \approx 6.9$.

7.2.2. Nonlinear evolution

Unlike for the 1D case, in the 2D nonlinear regime closed form solitary wave solutions of the CME are not known. Although a limited set of such solutions has been found numerically [11,10], here we use a heuristically selected initial condition that is close to a solitary wave and results in a much slower diffraction than in the linear regime as well as in co-propagation of energy carried by E_+ and E_- in the same z-direction. Of course, radiation waves are present as the solution is not a true solitary wave. The initial data we use are

$$\begin{pmatrix} E_+(x,z,0) \\ E_-(x,z,0) \end{pmatrix} = \sqrt{2} GS(z, 0; v = 0.92, \delta = \pi/2, z_0 = L_z/2) \operatorname{sech}(b(x - L_x/2)),$$

where $b = 2\kappa(\sin(\delta)/\delta - \cos(\delta))$ and GS is the gap soliton (21) centered at $z = L_z/2$, with velocity $v = 0.92$ and detuning $\delta = \pi/2$, see Fig. 24. We use $\Gamma = 1$, $L_z = 6$, $L_x = 12$, $dz = 0.04$, $dx = 0.08$ and $dt = 0.004$. The PML parameters are $a_z = 9.6/\delta_z$, $a_x = 16/\delta_x$ and $\delta_x = 2\delta_x = 1.6$, 2, 2.4, 2.8 and 3.2.

Figs. 25 and 26 show the solution modulus at $t = 2$ and $t = 4$, respectively. At $t = 2$ the main pulse is still within the physical domain and at $t = 4$ it has entered the z-layer as well as slightly diffracted into the x-layers. The approximate error convergence rates found by using the relation (22) with $\delta_x^{(1)} = 2\delta_z^{(1)} = 2.4$, $\delta_x^{(2)} = 2\delta_z^{(2)} = 2.8$ and $\delta_x^{(3)} = 2\delta_z^{(3)} = 3.2$ are $p \approx 3.1$ at $t = 2$ and $p \approx 1.4$ at $t = 4$. The fact that the decrease in the rate as the pulse enters the layer is not as dramatic as in the 1D case (Figs. 16 and 18) is attributed to the relatively small amplitude of the pulse as it enters the layer.

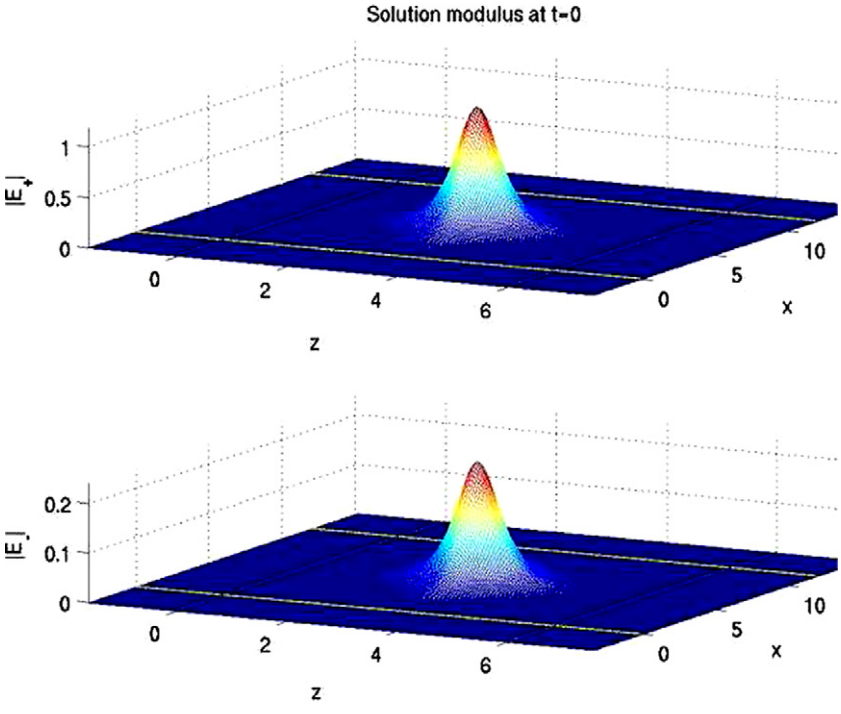

Fig. 24. Initial data.

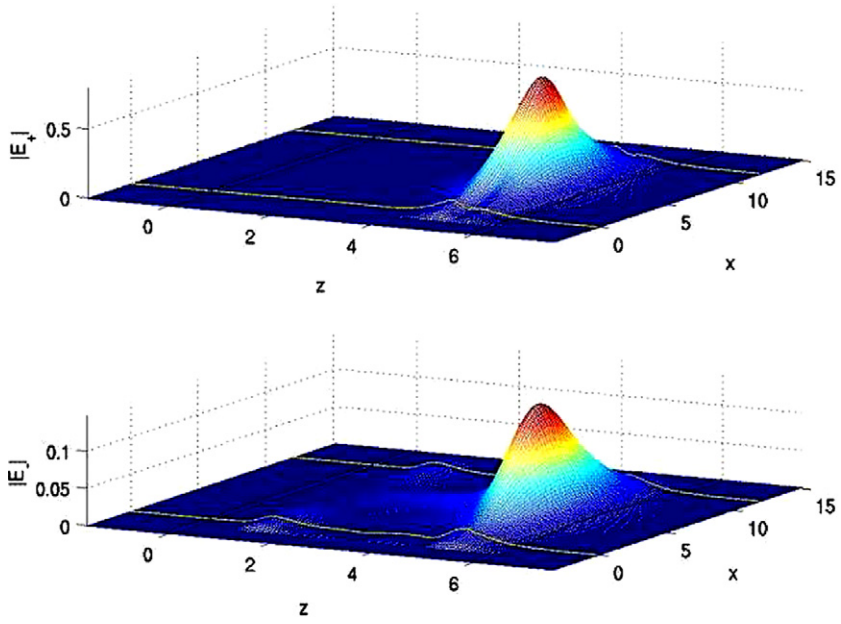

Fig. 25. Solution modulus at $t = 2$ for $\delta_x = 2\delta_z = 3.2$.

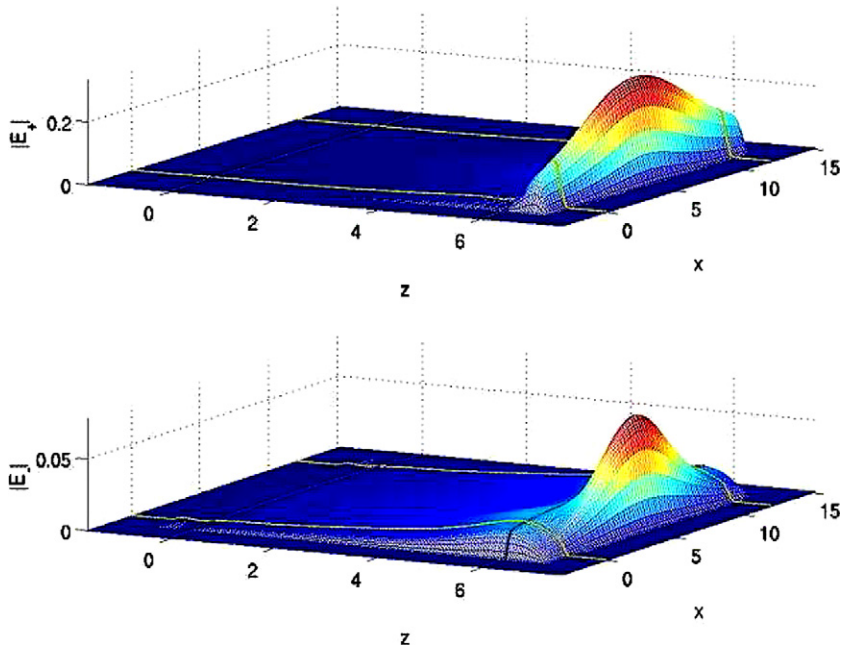

Fig. 26. Solution modulus at $t = 4$ for $\delta_x = 2\delta_z = 3.2$.

8. Conclusion

We have constructed PML equations for the mixed-type system governing propagation of optical wave packets in both 1D and 2D Bragg resonant photonic waveguides with a cubic nonlinearity, i.e. the coupled mode equations. The construction builds on an existing approach for general first order hyperbolic systems. The given analysis proves the desired absorption of the layers, their perfect matching as well as stability for the

corresponding linear system. Via performing a number of numerical FDTD simulations we verify the analytical results and show that the error due to layer truncation converges exponentially with respect to the layer width even in the nonlinear regime although at a decreased rate compared to the linear regime. An important topic for continuation of this work is construction of PML equations for other types of coupled mode equations in 2D photonic crystals, as classified in [3].

Acknowledgments

This research was supported in part by NSF Grant DMS-0306285, ARO Grant DAAD19-03-1-0146 and ARO Grant DAAD19-03-1-0209. Any conclusions or recommendations expressed in this paper are those of the authors and do not necessarily reflect the views of NSF or ARO. The authors thank Prof. A. Aceves of the University of New Mexico for fruitful discussions about the PDE model.

References

[1] A.B. Aceves, B. Costantini, C. De Angelis, Two-dimensional gap solitons in a nonlinear periodic slab waveguide, J. Opt. Soc. Am. B 12 (1995) 1475–1479.
[2] A.B. Aceves, S. Wabnitz, Self induced transparency solitons in nonlinear refractive media, Phys. Lett. A 141 (1989) 37–42.
[3] D. Agueev, D. Pelinovsky, Modeling of wave resonances in low-contrast photonic crystals, SIAM J. Appl. Math. 65 (4) (2005) 1101–1129 (electronic).
[4] N. Aközbek, S. John, Optical solitary waves in two and three dimensional photonic bandgap structures, Phys. Rev. E 57 (1998) 2287–2319.
[5] D. Appelö, T. Hagstrom, G. Kreiss, Perfectly matched layers for hyperbolic systems: General formulation, well-posedness and stability, SIAM J. Appl. Math. (to appear).
[6] I.V. Barashenkov, D.E. Pelinovsky, E.V. Zemlyanaya, Vibrations and oscillatory instabilities of gap solitons, Phys. Rev. Lett. 80 (1998) 5117–5120.
[7] W. Chen, D.L. Mills, Gap solitons and the nonlinear optical response of superlattices, Phys. Rev. Lett. 58 (1987) 160–163.
[8] A. de Hoop, P. van den Berg, R. Remis, Absorbing boundary conditions and perfectly matched layers – an analytic time-domain performance analysis, IEEE Trans. Magn. 38 (2002) 657–660.
[9] J. Diaz, P. Joly, A time-domain analysis of PML models in acoustics, Comput. Meth. Appl. Mech. Eng. 195 (2006) 3820–3853.
[10] T. Dohnal, Optical bullets in (2+1)D photonic structures and their interaction with localized defects, Ph.D. Thesis, University of New Mexico, Albuquerque, NM, USA, 2005.
[11] T. Dohnal, A.B. Aceves, Optical soliton bullets in (2+1)D nonlinear Bragg resonant periodic geometries, in: J. Yang (Ed.), Nonlinear Wave Phenomena in Periodic Photonic Structures, Studies in Applied Mathematics, vol. 115, 2005, pp. 209–232.
[12] C. Farrell, U. Leonhardt, The perfectly matched layer in numerical simulations of nonlinear and matter waves, J. Opt. B 7 (2005) 1–4.
[13] T. Fevens, H. Jiang, Absorbing boundary conditions for the Schrödinger equation, SIAM J. Sci. Comput. 21 (1999) 255–282.
[14] T. Fujisawa, M. Koshiba, Full-vector finite-element beam propagation method for three-dimensional nonlinear optical waveguides, Electron. Commun. Jpn., Part 2, 86 (2) (2003) 19–27, 200.
[15] R.H. Goodman, M.I. Weinstein, P.J. Holmes, Nonlinear propagation of light in one-dimensional periodic structures, J. Nonlinear Sci. 11 (2) (2001) 123–168.
[16] T. Hagstrom, Radiation boundary conditions for the numerical simulation of waves, in: Acta Numerica, 1999, Acta Numer., vol. 8, Cambridge University Press, Cambridge, 1999, pp. 47–106.
[17] T. Hagstrom, A new construction of perfectly matched layers for hyperbolic systems with applications to the linearized Euler equations, in: G. Cohen, E. Heikkola, P. Joly, P. Neittaanmäki (Eds.), Mathematical and Numerical Aspects of Wave Propagation Phenomena, Springer, Berlin, 2003, pp. 125–129.
[18] T. Hagstrom, New results on absorbing layers and radiation boundary conditions, in: M. Ainsworth, P. Davies, D. Duncan, P. Martin, B. Rynne (Eds.), Topics in Computational Wave Propagation, Springer, Berlin, 2003, pp. 1–42.
[19] T. Hagstrom, D. Appelö, Automatic symmetrization and energy estimates using local operators for partial differential equations, Comm. Part. Diff. Eq. (to appear).
[20] S. Jiang, Fast evaluation of nonreflecting boundary conditions for the Schrödinger equation, Ph.D. Thesis, New York University, 2001.
[21] C.A. Kennedy, M.H. Carpenter, Additive Runge–Kutta schemes for convection–diffusion-reaction equations, NASA-2001-TM211038 Technical Report Server, NASA Langley, 2001.
[22] C. Lubich, A. Schädle, Fast convolution for non-reflecting boundary conditions, SIAM J. Sci. Comput. 24 (2002) 161–182.
[23] D.E. Pelinovsky, A. Scheel, Stability analysis of stationary light transmission in nonlinear photonic structures, J. Nonlinear Sci. 13 (2003) 347–396.
[24] B. Sjogreen, N.A. Petersson, Perfectly matched layers for Maxwell's equations in second order formulation, J. Comput. Phys. 209 (1) (2005) 19–46.
[25] R.E. Slusher, B.J. Eggleton, Nonlinear Photonic Crystals, Springer, Berlin, 2003.

[26] J. Xu, J.-G. Ma, Z. Chen, Numerical validations of a nonlinear PML scheme for absorption of nonlinear electromagnetic waves, IEEE Trans. Microwave Theory Tech. 46 (11) (1998) 1752–1758.
[27] T. Yasui, M. Koshiba, A wide angle finite element beam propagation method with perfectly matched layers for nonlinear optical waveguides, J. Lightwave Technol. 17 (10) (1999) 1909–1915.
[28] A.P. Zhao, Application of the material-independent PML absorbers to the FDTD analysis of electromagnetic waves in nonlinear media, Microwave Opt. Technol. Lett. 17 (3) (1998) 164–168.